



1 **Advantages of assimilating multi-spectral satellite retrievals of atmospheric composition: A**
2 **demonstration using MOPITT CO products**

3
4 **Wenfu Tang¹, Benjamin Gaubert¹, Louisa K. Emmons¹, Daniel Ziskin¹, Debbie Mao¹, David**
5 **P. Edwards¹, Avelino F. Arellano², Kevin Raeder³, Jeffrey L. Anderson³, and Helen M.**
6 **Worden¹**

7
8 ¹Atmospheric Chemistry Observations & Modeling Laboratory, National Center for Atmospheric
9 Research, Boulder, CO, USA

10 ²Dept. of Hydrology and Atmospheric Sciences, University of Arizona, Tucson, AZ, USA

11 ³Computational and Information Systems Laboratory, National Center for Atmospheric Research,
12 Boulder, CO, USA

13
14 Correspondence: Wenfu Tang (wenfut@ucar.edu)

15
16 **Abstract**

17 The Measurements Of Pollution In The Troposphere (MOPITT) is an ideal instrument to
18 understand the impact of (1) assimilating multispectral/joint retrievals versus single-spectral
19 products, (2) assimilating satellite profile products versus column products, and (3) assimilating
20 multispectral/joint retrievals versus assimilating individual products separately. We use the
21 Community Atmosphere Model with chemistry with the Data Assimilation Research Testbed
22 (CAM-chem+DART) to assimilate different MOPITT CO products to address these three
23 questions. Both anthropogenic and fire CO emissions are optimized in the data assimilation
24 experiments. The results are compared with independent CO observations from TROPospheric
25 Monitoring Instrument (TROPOMI), the Total Carbon Column Observing Network (TCCON),
26 NOAA Carbon Cycle Greenhouse Gases (CCGG) sites, In-service Aircraft for a Global Observing
27 System (IAGOS), and Western wildfire Experiment for Cloud chemistry, Aerosol absorption and
28 Nitrogen (WE-CAN). We find that (1) assimilating the MOPITT joint (multispectral Near-IR and
29 Thermal-IR) column product leads to better model-observation agreement at and near the surface
30 than assimilating the MOPITT Thermal-IR-only column retrieval. (2) Assimilating column
31 products has a larger impact and improvement for background and large-scale CO compared to
32 assimilating profile products due to vertical localization in profile assimilation. However, profile
33 assimilation can out-perform column assimilations in fire-impacted regions and near the
34 surface. (3) Assimilating multispectral/joint products results in similar or slightly better agreement
35 with observations compared to assimilating the single-spectral products separately.

36
37
38 **1 Introduction**

39 With the increasing availability of satellite remote sensing instruments measuring
40 atmospheric composition, there is potential to produce multispectral retrievals of several species,
41 making use of thermal-infrared (TIR) and near-infrared (NIR) radiances from collocated
42 instruments on the same satellite such as IASI (Infrared Atmospheric Sounding Interferometer)
43 and GOME-2 (Global Ozone Monitoring Experiment-2) on the European MetOp satellites (Cuesta
44 et al., 2013), or flying in close formation, such as on the NASA A-train and the NOAA's JPSS
45 (Joint Polar Satellite System), e.g., OMI (Ozone Monitoring Instrument, Levelt et al., 2018), AIRS



46 (Atmospheric Infrared Sounder, Fu et al., 2018), OMPS (Ozone Mapping and Profiler Suite, Flynn
 47 et al., 2014), TROPOspheric Monitoring Instrument (TROPOMI, Veeffkind et al., 2012) and CrIS
 48 (Cross-track Infrared Sounder, Fu et al., 2016). TIR retrievals use thermal contrast while NIR
 49 retrievals use reflected solar radiance from the surface. Taking MOPITT as an example, the TIR
 50 retrieval can provide vertical profiles with limited sensitivity to the surface while the NIR retrieval
 51 only provide total column product with some sensitivity to the surface. An example of averaging
 52 kernels of the MOPITT TIR and NIR retrievals can be found in the Figure 2 of Worden et al.
 53 (2010).

54 The multispectral products have shown considerable increases in the vertical sensitivity of
 55 the retrievals for lowermost tropospheric ozone (O₃) (e.g., Worden et al., 2007; Natraj et al., 2011;
 56 Fu 2018), carbon monoxide (CO) (Worden et al., 2010; Fu et al., 2016) and methane (CH₄)
 57 (Schneider et al. 2022). Multispectral retrievals could be made using the co-located overpass made
 58 by low earth orbit and geostationary satellite such as, e.g., Geostationary Interferometric Infrared
 59 Sounder (GIIRS, Zeng et al., 2023), Geostationary Environment Monitoring Spectrometer
 60 (GEMS, Kim et al., 2020) and Tropospheric emissions: Monitoring of pollution (TEMPO, Chance
 61 et al., 2019). Table 1 shows the developed and potential multispectral products. It is important to
 62 understand the value of assimilating a multispectral product versus assimilating a single-spectral
 63 range product, and the value of assimilating a multispectral product versus separately assimilating
 64 single-spectral range products that are used to retrieve the multispectral products.
 65

66 **Table 1.** Developed and potential multispectral satellite retrievals. Shown in the table are satellites,
 67 their NIR and/or TIR spectral ranges (in μm), and potential chemical species from the multispectral
 68 retrievals.

Morning Overpass	Afternoon Overpass	Geostationary
MOPITT (2.3 & 4.7)	AIRS (3.75–15.4) + OMI (0.27–0.5)	GIIRS (East Asia) (0.55–14.2) + TROPOMI (2.3–2.4)
(CO)	(O ₃)	
IASI (3.6–15.5) + GOME2 (0.24–0.79)	TES (8.7–10.5) + OMI (0.27–0.5)	GEMS (East Asia) (0.3–0.5) + IASI (3.6–15.5)
(O ₃)	(O ₃)	
	GOSAT (0.75–15) + TES (8.7–10.5)	GEMS (East Asia) (0.3–0.5) + CrIS (3.9–15.4)
	CrIS (3.9–15.4) + GOSAT-2 (0.3–14.3)	TEMPO (N. America)+ IASI (3.6– 15.5)
	(CO, CH ₄)	
	CrIS (3.9–15.4) + TROPOMI (2.3–2.4)	TEMPO (N. America)+ CrIS (3.9– 15.4)
	(CO, O ₃ , CH ₄)	

69
 70 Total column observations of ozone, CO and NO₂ are now routinely assimilated in
 71 operational centers such as in the European Copernicus Atmosphere Monitoring Service (CAM5)
 72 program at the European Centre for Medium-Range Weather Forecasts (Inness et al., 2019; 2022)
 73 In addition, recently launched geostationary satellites such as GEMS and TEMPO will provide
 74 column products at high temporal resolution. While the satellite profile products are in general
 75 considered to contain more vertical information, it is important to understand the impacts of
 76 assimilating column products versus assimilating profile products and to understand what
 77 information is potentially missed by only assimilating column products. For example, Jiang et al.
 78 (2017) compared emission updates following the assimilation of the MOPITT lowermost surface
 79 profile, the tropospheric profile or the columns and identified errors indicative of model transport
 80 error impacts on emission estimates.

81 The Measurements of Pollution in the Troposphere (MOPITT) instrument onboard the
 82 NASA Terra satellite is an ideal instrument to address these three questions. MOPITT retrieves



83 total column amounts and vertical profiles of CO using both thermal-infrared (TIR) and near-
84 infrared (NIR) measurements. In addition, MOPITT also provides the multispectral TIR-NIR joint
85 product, which has enhanced the sensitivity to near-surface CO (Deeter et al., 2011, 2013; Worden
86 et al., 2010). By comparing the results of assimilating different combinations of MOPITT CO
87 products, we will be able to address these two questions.

88 To conduct the data assimilation experiments, we use the Community Atmosphere Model
89 with chemistry and the Data Assimilation Research Testbed (Anderson et al., 2009). CAM-
90 chem+DART has been previously used to assimilate MOPITT profile products (Arellano et al.,
91 2007; Barré et al., 2015; Gaubert et al., 2016, 2017, 2020, 2023). Here we present the first
92 assimilation of MOPITT column products within CAM-chem+DART. This new capability also
93 allows us to assimilate other satellite column products of CO and other chemical species in the
94 future. Anthropogenic and fire emissions are optimized separately in the data assimilation
95 experiments.

96 This paper aims to understand the impacts of (1) assimilating multispectral/joint products
97 versus single-spectral products, (2) assimilating satellite profile products versus column products,
98 and (3) assimilating multispectral/joint products versus assimilating individual products
99 separately. The paper is organized as follows: Section 2 describes CAM-chem, DART, and
100 methods, Section 3 describes datasets used for results evaluation, Section 4 presents data
101 assimilation results, Section 5 shows comparisons between data assimilation results and
102 independent observations, Section 6 discuss optimized emissions and CAM-chem simulations
103 with updated emissions, Section 7 is discussion and Section 8 concludes the study.

104
105
106

107 **Section 2: Methods and data**

108 **2.1 MOPITT products**

109 The Measurements of Pollution in the Troposphere (MOPITT) instrument on board the
110 NASA Terra satellite provides both thermal-infrared (TIR) and near-infrared (NIR) radiance
111 measurements since March 2000 (Deeter et al., 2003). CO total column amounts and volume
112 mixing ratio (VMR) profiles (10 vertical layers) are retrieved from the radiance measurements.
113 TIR is used to retrieve MOPITT TIR CO total column product and MOPITT TIR CO vertical
114 profile product; NIR is used to retrieve MOPITT NIR CO column product. Besides the TIR-only
115 and NIR-only products, multispectral (JNT) products are also provided by MOPITT by jointly
116 retrieving from TIR and NIR. JNT retrievals provide both MOPITT JNT CO total column product
117 and MOPITT JNT CO vertical profile product. JNT products have enhanced the sensitivity to near-
118 surface CO (Deeter et al., 2011, 2013; Worden et al., 2010). MOPITT products can be accessed
119 through <https://search.earthdata.nasa.gov/search>. In this study, we assimilate daytime MOPITT
120 version 9 products (Deeter et al., 2022) of TIR profile, TIR column, NIR column, JNT profile, and
121 JNT column in our experiments.

122 We use the error-weighted average of the MOPITT data within $1^\circ \times 1^\circ$ model grid and 6-
123 hourly bin (i.e., super-observations). Averaged daily numbers of daytime total super-observations
124 from MOPITT TIR, NIR, and JNT products during July 16th 2018 to August 14th 2018 is shown
125 in Figure 1. The NIR product only covers the land while TIR and JNT products cover the land and
126 ocean. Over the ocean, the JNT product is the same as the TIR product (Worden et al., 2010).

127
128

128 **2.2 CAM-chem**



129 The Community Earth System Model (CESM) is a global Earth system model that includes
130 the atmosphere, land, ocean, and ice components (Danabasoglu et al., 2020). CAM-chem;
131 (Emmons et al., 2020; Tilmes et al., 2019) is a global chemistry-climate model as a configuration
132 of CESM version 2.2 (<https://www2.acom.ucar.edu/gcm/cam-chem>). CAM-chem accounts for
133 physical, chemical and dynamical processes with a spatial resolution of 1.25° in longitude and
134 0.95° in latitude and 32 vertical layers with ~8 layers in boundary layer and ~10 layers in the free
135 troposphere (Tang et al., 2023). We use the default MOZART-TS1 chemical mechanism, which
136 includes comprehensive tropospheric and stratospheric chemistry with ~220 chemical species and
137 528 reactions (Emmons et al., 2020). The aerosol scheme used is the four-mode version of the
138 Modal Aerosol Module (MAM4; Liu et al., 2016).

139 We use CAMS-GLOB-ANT v5.1 inventory (Soulie et al., 2023) for anthropogenic
140 emissions and FINNv2.4 (Wiedinmyer et al., 2023) for fire emissions. CAMS-GLOB-ANT v5.1
141 provide monthly emissions and we generated daily files from the interpolation of the monthly
142 values. The FINNv2.4 inventory provide daily fire emissions and are used directly. We update CO
143 emission input files using the relative surface flux increments at every MOPITT CO assimilation
144 step (6-hourly).

145

146 2.3 DART

147 DART is an open-source community facility for efficient ensemble data assimilation
148 (<https://dart.ucar.edu/>). It is developed and maintained at the National Center for Atmospheric
149 Research (NCAR). DART has been coupled with Community Atmosphere Model (CAM) for
150 global meteorological data assimilation (CAM+DART; Raeder et al., 2012, 2021). Based on
151 CAM+DART, the capability of chemical data assimilation using CAM-chem online chemistry and
152 DART is developed and applied for scientific research (CAM-chem+DART; Arellano et al., 2007;
153 Barré et al., 2015; Gaubert et al., 2016, 2017, 2020). To assimilate meteorology and chemical
154 observational data, an ensemble of 30 CAM-chem simulations with different initial conditions and
155 emissions to generate the forecast ensemble at a given time. DART assimilates observations and
156 produce the analysis, an ensemble of optimized initial conditions (see details in Gaubert et al.,
157 2016). We use ensemble mean at the forecast and the analysis step in the result sections. Ensemble
158 mean of forecast is denoted by

$$159 \quad \overline{x^f} = \frac{1}{N} \sum_{j=1}^N x_j^f \quad (1)$$

160

161 Where $\overline{x^f}$ is the ensemble mean of “forecast”, N is the ensemble size and x_j^f is the forecast value
162 of the j-th ensemble member. In our runs, DART uses the Ensemble Adjustment Kalman Filter
163 (EAKF; Anderson et al., 2001, 2003), a deterministic ensemble square root filter for the analysis
164 step. Unless noted otherwise, our setup is the same as in Gaubert et al., (2023). We slightly change
165 the emission update to include a correction to the previous day (t-1) in order to smooth the
166 emissions increments. Briefly, we apply multiplicative covariance inflation to the forecast
167 ensemble before each analysis step to optimally adjust the ensemble spread. The inflation
168 parameter is also sequentially updated (Gharamti 2018) and varies in both space and time. The
169 spatial localization horizontal half width is 600 km and 1200 m vertically. The main difference
170 between the profile and the column assimilation resides in the vertical localization. There is no
171 vertical localization in the column data assimilation except that the stratospheric (top 5) levels are
172 not updated, as in the CO profile and meteorological DA.

173 Forward operators (denoted as H) are applied to project model field to observation space
174 (i.e., expected observations). In this case, the forward operators apply MOPITT averaging kernel



175 and prior information to model CO field before comparing it to MOPITT products. The capability
176 of assimilating MOPITT profile products is described in Barré et al., (2015). In this study, we
177 introduce observation operator to assimilate the MOPITT columns DART.

178 We estimate the retrieved column C (molecules cm^{-2}), using the prior column C_a and
179 following Equation 3 of the MOPITT Version 9 Product User's Guide:

$$180 \quad C = C_a + a(x_{CAM-chem} - x_a) \quad (2)$$

181 Where $x_{CAM-chem}$ and x_a are the modelled and the a priori profiles expressed as $\log_{10}(\text{VMR})$ and
182 a is the total column averaging kernel. In this study, we assimilate both MOPITT profile and
183 column products and compare the results.

184

185 **2.4 Data assimilation experiments setup**

186 There are 6 CAM-chem+DART runs (Figure 2). The first run is the spin-up/control run
187 that starts on July 1st 2018. The spin-up/control run only assimilates meteorological observations
188 and the state vector consists in wind, temperature, specific humidity, and surface pressure. Besides
189 the spin-up/control run, there are 5 experiment runs that assimilate different MOPITT CO
190 product(s) to update model CO. Note that the experiment runs not only assimilate MOPITT CO
191 products but also meteorological variables as in the spin-up/control run. The chemical state vector
192 (CO and CO emissions) and the meteorological state vector do not impact each other. However,
193 the changed meteorology due to meteorological data assimilation will impact the transport and
194 possibly chemistry of CO during the forecast step. The 5 experiment runs are:

- 195 (1) Column JNT assimilation;
- 196 (2) Profile JNT assimilation;
- 197 (3) Column TIR assimilation;
- 198 (4) Column TIR and column NIR assimilation;
- 199 (5) Profile TIR and column NIR assimilation.

200 These 5 experiment runs are designed to address a few scientific questions:

- 201 • The comparisons of experiment (1) and (2) will show the impacts of the assimilation of
202 satellite profile versus column products.
- 203 • The comparisons of experiment (1) and (3) will show the difference caused by TIR-only
204 product versus joint product.
- 205 • The comparisons of experiment (1) and (4) will show the impacts of assimilating joint
206 products (TIR+NIR) versus assimilating them separately for column products.
- 207 • The comparisons of experiment (2) and (5) will show the impacts of assimilating joint
208 products (TIR+NIR) versus assimilating them separately for profile products.

209 The experiment runs starts on July 16th 2018 and are initialized with the spin-up/control
210 run. Each experiment runs for 35 days considering the cost and constrain of computational
211 allocation. The first 20 days (July 11th to July 15th, 2018) are CO spin-up and the last 15 days (July
212 31st to August 14th, 2018) are used for result analyses. The 15-day period are selected based on the
213 spin-up time – as shown by fractions of observations rejected by the assimilation system (Figure
214 3), the experiments finished spinning up around 31 July. Each CAM-chem+DART run includes
215 30 ensemble members. These 30 ensemble members have different initial conditions and emissions
216 to represent model uncertainties. The analysis step is done every 6 hours. Anthropogenic and fire
217 emissions are optimized separately on a daily basis following the method described in Gaubert et
218 al. (2020, 2023).

219

220 **2.5 CAM-chem simulations with updated emissions**



221 To evaluate the updated emissions from the DA experiments, we conduct CAM-chem
222 simulations for the same period using the ensemble mean of the updated fire and anthropogenic
223 emissions. Hourly output is used for these simulations. Specifically, we conduct 6 CAM-chem
224 simulations:

- 225 (S1) Simulation with emissions from (1) Column JNT assimilation;
- 226 (S2) Simulation with emissions from (2) Profile JNT assimilation;
- 227 (S3) Simulation with emissions from (3) Column TIR assimilation;
- 228 (S4) Simulation with emissions from (4) Column TIR and column NIR assimilation;
- 229 (S5) Simulation with emissions from (5) Profile TIR and column NIR assimilation;
- 230 (SControl) Simulation with original CAMS and FINN emissions.

231

232 **3 Datasets used for results evaluation**

233

234 **3.1 TROPospheric Monitoring Instrument (TROPOMI)**

235

236 We use CO column retrieved from the TROPOMI instrument onboard the ESA's Sentinel-
237 5 Precursor (Veeffkind et al., 2012) to evaluate model results. The spatial resolution of CO
238 retrievals is $\sim 5.5 \text{ km} \times 7 \text{ km}$ (Veeffkind et al., 2012; Borsdorff et al., 2018). TROPOMI CO data
239 can be downloaded from <https://s5phub.copernicus.eu/dhus/#/home>. The TROPOMI Level 2 CO
240 (Apituley et al., 2018) is used here. The TROPOMI data are filtered following Landgraf et al.
241 (2018). To compare the model results with TROPOMI CO, we interpolate model outputs spatially
242 and temporally to match the locations and times of TROPOMI CO retrievals, and then apply
243 TROPOMI CO total column averaging kernels to the interpolated model CO profiles to obtain
244 modeled total CO columns (Apituley et al., 2018).

244

245 **3.2 The Total Carbon Column Observing Network (TCCON)**

246

247 TCCON is a network of ground-based Fourier Transform Spectrometers that records direct
248 solar spectra in the NIR spectral region. Column-averaged mixing ratios of chemical species such
249 as CO₂, CH₄, N₂O, and CO are retrieved from these spectra. We use CO column data from the
250 TCCON GGG2020 data release (<https://tccondata.org/2020>; TCCON Team, 2022) to evaluate
251 model results. We interpolate model results to TCCON data locations and time and apply TCCON
252 averaging kernels to model results for proper comparisons.

252

253 **3.3 NOAA Carbon Cycle Greenhouse Gases (CCGG) sites**

254

255 We use the atmospheric CO dry air mole fractions from the NOAA GML Carbon Cycle
256 Cooperative Global Air Sampling Network (https://gml.noaa.gov/aftp/data/trace_gases/co/flask/surface/; Petron et al., 2022). Event data are
257 used. The reference scale is WMO CO_X2014A. We interpolate model results to CCGG site
258 locations and time for proper comparisons. Note that on average, each site only has data on ~ 4
259 days and ~ 9 data points in total from July 16th, 2018 to August 14th, 2018.

260

261 **3.4 In-service Aircraft for a Global Observing System (IAGOS)**

262

263 IAGOS is a European research infrastructure developed for operations on commercial
264 aircraft to monitor atmospheric composition (Petzold et al., 2015). The IAGOS instrument package
265 1 measures CO as well as O₃, air temperature, and water vapor (<https://www.iagos.org/iagos-core-instruments/package1/>). CO is measured by infrared absorption using the gas filter correlation
266 technique (Precision: $\pm 5\%$, Accuracy: $\pm 5 \text{ ppb}$). Here we use vertical profiles of CO from IAGOS



267 for model evaluation. We use CO profiles in North and West Africa, Tropical Asia, East Asia,
268 Europe, Eastern North America, Western North America, Central and South America, and Middle
269 East and conduct evaluation in these regions separately. CO profiles used and regions is shown in
270 Figure S2. Note that IAGOS profiles are divided into regions based on their locations, however
271 the IAGOS profiles in a region are not representative of the whole region due to coverage (Figure
272 S2).

273

274 **3.5 Western wildfire Experiment for Cloud chemistry, Aerosol absorption and Nitrogen** 275 **(WE-CAN)**

276 The WE-CAN field campaign was conducted over the Northwestern U.S. during July–
277 September 2018 (<https://data.eol.ucar.edu/project/WE-CAN>). There were 16 research flights of
278 the NCAR/NSF C-130 research aircraft during the campaign. Our experiment runs start on July
279 16th and end on August 14th. Therefore, we compare the model results to measurements from
280 flights on July-31, August-02, August-03, August-06, August-08, August-09, and August-13. We
281 use 1-minute averaged CO (Picarro G2401-mc) data. Model results are interpolated to match
282 locations and time of the observations, and then both interpolated model results and observations
283 are averaged back to the model spatial resolution (1.25° in longitude and 0.95° in latitude), 6-
284 hourly bins, and 50 hPa vertical layers. This is because the model spatial and temporal resolution
285 are much lower than observations and model results cannot reproduce the high variability in the
286 raw observations.

287

288 **4. Results**

289 **4.1 Observation space diagnostics**

290 **4.1.1 Fractions of observations rejected by the assimilation system**

291 In all the five experiments, the assimilation improves the agreement between model
292 forecast and observations of not only the MOPITT products assimilated but also the MOPITT
293 products that were not assimilated. Assimilating MOPITT CO column product(s) improves model
294 agreement with MOPITT CO profile product(s) and vice versa. Figure 3 shows time series of the
295 fraction of observations rejected by the assimilation system (%) when they are too far from the
296 model ensemble mean. The decreasing fractions with time indicate more observations being
297 accepted by the model, i.e., and observations and modeled values are getting closer in later time
298 steps. For a MOPITT product that is not assimilated in an experiment run, it is still used in the
299 “evaluation mode”, where the ensemble is run through the observation operator, but not
300 assimilated. Therefore, the hypothetical fraction of observations rejected is still calculated for the
301 MOPITT product for that experiment run, even though these observations are not assimilated. For
302 the spin-up/control run, there is no significant trend for the fractions of rejected observations
303 (Figure 3f). For the five experiments, the fractions of rejected observations decrease with time.
304 Assimilating (Figures 3a-3e) any MOPITT product(s) improves model agreement with all the five
305 MOPITT CO products regardless if they are column or profile products. When only assimilating
306 column products ((1) Column JNT assimilation; (3) Column TIR assimilation; and (4) Column
307 TIR and column NIR assimilation), the fraction of rejected observations decreases faster than that
308 when assimilating both profile and column products ((5) Profile TIR and column NIR
309 assimilation). For experiments that assimilate profiles (Experiments (2) and (5)), the fractions of
310 rejected observations decrease slower than the other three experiments that only assimilate column
311 products (Experiments (1), (3), and (4)). This is expected because profile assimilation has
312 relatively small impact than column assimilation overall due to vertical localization.



313

314 **4.1.2 Reduced centered random variable (RCRV) and chi-square statistics χ^2**

315 We use the RCRV as a diagnostic of the ensemble bias (Candille et al., 2007) and has been
316 previously used to validate assimilation results (e.g., Gaubert et al., 2014). Mean RCRV for P
317 observations is defined by the ratio between the innovation and its associated error:

$$318 \quad RCRV = \frac{1}{P} \sum_{i=1}^P \frac{y_i^o - Hx_i^f}{\sqrt{\sigma_{o,i}^2 + \sigma_{f,i}^2}} \quad (3)$$

319 Where y_i^o is the value of i-th observation, Hx_i^f gives the expected observation from the model $\sigma_{o,i}^2$
320 is the observation error variance, and $\sigma_{f,i}^2$ is the ensemble variance. The mean of the RCRV
321 represents the weighted bias of the forecast, and hence a value close to 0 indicates the ensemble is
322 representative (i.e., error variances are comparable to the innovations). Figure 4 shows daily
323 \overline{RCRV} . For a given experiment, only \overline{RCRV} of MOPITT product(s) assimilated in the experiment
324 is shown here. In most cases \overline{RCRV} is close to zero, indicating that the ensemble is representative.
325 The only exceptions are NIR column product in (4) Column TIR and column NIR assimilation and
326 (5) Profile TIR and column NIR assimilation.

327 Chi-square statistics (χ^2) is also used to verify an effective assimilation by comparing error
328 specifications and their balance with actual model-observation mismatch (Ménard and Chang,
329 2000) and has been previously used to evaluate assimilation results (e.g., Gaubert et al., 2016;
330 Sekiya et al., 2021). Mean RCRV for P observations is defined as

$$331 \quad \overline{\chi^2} = \frac{1}{P} \sum_{i=1}^P \frac{(y_i^o - Hx_i^f)^2}{\sigma_{o,i}^2 + \sigma_{f,i}^2} \quad (4)$$

332 A value lower than 1 indicates an overfitting of the observations while a value higher than 1
333 suggests an underestimation of the actual model and observation mismatch. Daily $\overline{\chi^2}$ are also
334 shown in Figure 4. The $\overline{\chi^2}$ values are all higher than 1 indicating an underestimation of the actual
335 model and observation mismatch. However, $\overline{\chi^2}$ decreases with time and gradually approaches
336 towards 1, indicating the degree of such underestimation decreases with time.

337

338 **4.2 Model space diagnostics**

339 We analyze the impacts of assimilating MOPITT CO products by comparing the
340 experiment runs with control/spin-up run, which effectively isolate the signal resulting from the
341 CO assimilation. Figure 5 show the spatial distribution of CO difference caused by assimilation
342 (CO from forecast of experiment minus CO from the control/spin-up run) for the 5 experiments
343 (15-day average). At the surface, the spatial distributions of CO difference are similar among the
344 5 experiments. In line with Gaubert et al., 2023, the 5 experiments show overall higher CO in the
345 Northern Hemisphere and lower CO in the tropics and India compared to the control/spin-up run.
346 Experiment (2) Profile JNT assimilation and Experiment (5) Profile TIR and column NIR
347 assimilation reduce CO in California which is not the case for other experiments. Experiment (2)
348 Profile JNT assimilation and Experiment (5) Profile TIR and column NIR assimilation are the only
349 two experiments that involves profile product assimilation. In addition, profile JNT is retrieved
350 with profile TIR and column NIR therefore Experiment (2) Profile JNT assimilation is expected
351 to assimilate similar information as (5) Profile TIR and column NIR assimilation. In addition,
352 when comparing Experiments (1) and (2), column assimilation has a larger downwind impact (e.g.,
353 the ocean between Africa and South America). At 500 hPa, the 5 experiments still show overall
354 higher CO in the Northern Hemisphere compared to the control/spin-up run. However, the



355 Experiment (2) and (5) that include profile assimilation have lower CO values than the other 3
356 experiments, especially in the high latitudes.

357 Assimilating profile products have different vertical impacts from assimilating column
358 products (Figure 6). Overall, the two experiments that involve profile assimilation (Experiments
359 (2) and (5)) seem to be close to each other, while the other three experiments that only involve
360 column assimilation (Experiments (1), (3), and (4)) also exhibit similarities among themselves.
361 Globally speaking, experiments that assimilate only column product(s) have a larger impact at and
362 near the surface compared to experiments that assimilate only profile product(s) (Figures 6a and
363 6b). This is reasonable because profile assimilation is more localized vertically. Regional speaking,
364 the impacts of the five experiments vary across continents.

365 The difference caused by assimilating profile products is in general smaller than the
366 difference caused by assimilating column products. The exceptions are Africa and South America
367 where the two experiments that assimilate profiles have lower CO than the three experiments that
368 only assimilate columns between 900 hPa and 600 hPa. CO over the two regions is dominated by
369 fire emissions during the experiment period. It is known that FINN overestimates fire emissions
370 in the tropics (Wiedinmyer et al., 2023; Gaubert et al., 2023) of CO which were transported to
371 upper levels through fire plume rise and tropical convection. This overestimation between 900 hPa
372 and 600 hPa is corrected by assimilating MOPITT CO products, especially profile products that
373 captured CO plumes between 900 hPa and 600 hPa. Experiment (2) Profile JNT assimilation and
374 Experiment (5) Profile TIR and column NIR assimilation have some relatively small differences
375 over some regions even though profile JNT is retrieved with profile TIR and column NIR. For
376 example, over North America, (2) Profile JNT assimilation has lower CO values than Experiment
377 (5) Profile TIR and column NIR assimilation. Experiment (1) Column JNT assimilation and
378 Experiment (4) Column TIR and column NIR assimilation are in general similar with some
379 exceptions. For example, over Africa between 900 hPa and 600 hPa, CO profile from Experiment
380 (1) Column JNT assimilation is closer to Experiment (3) Column TIR assimilation rather than
381 Experiment (4) Column TIR and column NIR assimilation.

382

383 **5 Comparisons with independent observations**

384 **5.1 TROPOMI**

385 To evaluate the results, we compare the CO from DA forecasts with independent
386 observations. Comparisons with TROPOMI CO column retrievals are shown in Figure 7. The
387 control run underestimates background CO in the Northern Hemisphere while overestimates CO
388 near fire source regions in the tropics and Southern Hemisphere. Compared to the control run, all
389 five of the experiments show improved agreement with TROPOMI CO by increasing background
390 CO in the Northern Hemisphere and reducing CO near fire source regions in the tropics and
391 Southern Hemisphere. The spatial distributions of the mean biases from the three experiments with
392 only column assimilation are close while those from the two experiments with profile assimilation
393 are close. The two experiments with profile assimilations have smaller improvement for
394 background CO in the Northern Hemisphere. This is reasonable because profile assimilation has
395 relatively small impact than column assimilation due to tight vertical localization. However, near
396 the fire source regions, the two experiments with profile assimilations have lower biases than the
397 three experiments with only column assimilation. This is the case not only in Africa, South
398 America and tropical Asia (Figure 7), but also in California (fire region) and Nevada (downwind
399 of the fire region), USA during the study period which is the fire season in the region (Figure S5).
400 This indicates profile assimilation can out-perform column assimilations in circumstances with



401 fire impacts, which is likely due to transport errors and fire plume rise that requires vertical
402 information to resolve plume locations.

403

404

5.2 TCCON

405

406

407

408

409

410

411

412

413

414

Overall, the control run tends to underestimate CO and the 5 experiments all agree better with TCCON observations compared to the control run but still underestimates CO in general (Figure 8). Column assimilations (Experiments (1), (3), and (4)) significantly overestimate CO at pasadena01 and edwards01 sites in California, USA during 26 July 2018 to 04 August 2018, likely due to fire impacts. The significant overestimation is not seen in the two experiments with profile assimilations (Experiments (2) and (5)). This is consistent with the comparison results with TROPOMI and implies the profile assimilation can out-perform column assimilations in fire-impacted regions. The model-observation discrepancies overall decrease with time. A time series of TCCON and modeled CO columns is shown in Figure S6.

414

415

5.3 CCGG sites

416

417

418

419

420

421

422

423

424

All experiments show improved agreement with surface in-situ CO observations from CCGG sites compared to the control run (Figure 9), as shown by with higher correlations (0.6-0.65 versus 0.56) and lower model biases (0.7-4.91 ppb versus 8.6 ppb). As for RMSE, however, the experiments do not reduce RMSE compared to the control run (34-50 ppb versus 36 ppb). Experiment (1) Column JNT assimilation has the lowest mean bias (0.7 ppb) while Experiment (2) Profile JNT assimilation have the highest correlation (0.65). (1) Column JNT assimilation, (2) Profile JNT assimilation, (3) Column TIR assimilation, (4) Column TIR and column NIR assimilation, and (5) Profile TIR and column NIR assimilation.

424

425

426

427

428

429

430

431

Spatial distributions of model bias in CO (ppb) against CO observations from CCGG sites are shown in Figures S7-S10. The UTA CCGG site is close to the two TCCON sites in California, USA (pasadena01 and edwards01). All the five experiments significantly underestimate CO at the UTA surface site during 26 July 2018 to 4 August 2018, whereas the five experiments overestimate CO compared to the two TCCON sites (Figure 8). This inconsistency is likely due to (1) UTA CCGG site measures CO at the surface while the TCCON sites measure column total CO; (2) there are only two data points during that period at the UTA site and are not comparable to the sampling of the two TCCON sites.

432

433

5.4 IAGOS

434

435

436

437

438

439

440

441

442

443

444

445

446

Globally, all five experiments agree better with IAGOS CO profiles compared to the control run (Figure 10a). At the 900-1000 hPa layer, Experiment (2) Profile JNT assimilation has the lowest bias, followed by Experiment (4) Column TIR and column NIR assimilation. At layers above 800 hPa, the three experiments with only column assimilation have lower bias. CO bias of Experiments (1) Column JNT assimilation and (4) Column TIR and column NIR assimilation are very similar using that of (3) Column TIR assimilation as a reference. This is expected as Column JNT product contains similar information as column TIR product and column NIR products together. Over most regions, the five experiments show improved agreement with IAGOS data except for Tropical Asia and Central and South America where the five experiments have similar or larger biases (Figure 10). Over North and West Africa, the control run has positive bias whereas the five experiments have negative biases below 500 hPa, indicating the system might over-adjust in the region. The comparisons with IAGOS show that the experiments overall perform better in the Northern Hemisphere than in the tropics.



447

448 **5.5 WE-CAN**

449 The experiments do not show improvement from the control run when compared to
450 airborne measurements from WE-CAN. This is expected because the airborne measurements
451 during WE-CAN aimed to sample fire plumes and include extremely high CO concentrations
452 which are challenging for a 1-degree global model to capture, not to mention the output is 6-hourly.
453 The experiments only do show lower model bias than the control run (-24 to -48 ppb versus -52
454 ppb), however the difference between Experiments (2) and (5) from the control run is small. The
455 correlation and RMSE of the experiments are not improved. The subtle improvement in the mean
456 bias is likely driven by large-scale adjustment rather than improvement in resolving flight-scale
457 features.

458

459 **6. Emissions**

460 **6.1 Emission updates**

461 Assimilating profile products (Experiments (2) and (5)) tends to have a larger change to
462 the emissions compared to only assimilating column products (Experiments (1), (3), and (4)). The
463 5 experiments overall increase anthropogenic CO emissions while reduce fire CO emissions. For
464 anthropogenic emissions, the two experiments that assimilate CO profiles (Experiments (2) and
465 (5)) significantly increase anthropogenic CO emissions from ~500 Tg/year to ~700 Tg/year
466 globally in August, which is not the case for the other experiments. Anthropogenic emissions in
467 India are reduced by the experiments while in East Asia are increased (Figure 13). Fire emissions
468 are reduced by the 5 experiments in Africa and South America and the reduction is the largest for
469 the two experiments that assimilate CO profiles (Figures 12 and 13). This is consistent with the
470 conclusion in Wiedinmyer et al. (2023), which found fire emissions in FINNv2.4 over Africa are
471 too high, and consequently were reduced in FINNv2.5. The experiments overall increase fire
472 emissions in North America, indicating that FINNv2.4 underestimates fire emissions in the region
473 during the assimilation period. Fire and anthropogenic emissions can have different injection
474 heights and impact different vertical levels. This is especially the case for regions with strong
475 convection (e.g., central Africa).

476

477 **6.2 CAM-chem simulations with updated emissions**

478 We compared the CAM-chem simulations with updated emissions and original emissions
479 to CO observations from TROPOMI, TCCON, CCGG site, IAGOS, and WE-CAN (Figures S11-
480 S18). The five simulations with updated emissions overall show better agreement with
481 observations compared to the control run with original emissions. Simulations using emissions
482 from profile assimilation experiments (Simulations (S2) and (S5)) in general perform better than
483 column assimilation especially near the surface (S17) and at fire source regions (Figures S11, S12,
484 and S14). This is consistent with the evaluation of DA experiments. This indicates assimilating
485 satellite profiles can perform better near the surface and have a larger impact on emissions
486 compared to only assimilating column products.

487

488 **7. Discussions**

489 **7.1 Assimilating multispectral product versus TIR-only product**

490 The comparisons between experiment (1) Column JNT assimilation and (3) Column TIR
491 assimilation demonstrate the impacts of assimilating satellite multispectral/joint products versus
492 TIR-only products. Overall, when comparing to independent CO column observations,



493 assimilating joint products do not show clear improvement from assimilating TIR-only products
494 (Figures 7 and 8). However, when comparing to independent CO profile observations or surface
495 CO observations, assimilating joint products leads to better model-observation agreement at and
496 near the surface (Figures 9 and 10). This is reasonable as the joint MOPITT product has enhanced
497 sensitivity to near-surface CO (Worden et al., 2010).

498

499 **7.2 Assimilating profile product versus column product**

500 The comparisons between experiment (1) Column JNT assimilation and (2) Profile JNT
501 assimilation demonstrate the impacts of assimilating satellite multispectral/joint products versus
502 TIR-only products. The fractions of rejected observations for Experiment (3) decrease slower
503 than experiment (1) due to vertical localization when assimilating profile products. For the same
504 reason, assimilating column products has a larger impact on the analysis compared to assimilating
505 profile products. Therefore, experiment (2) with profile assimilation has smaller improvement for
506 background and large-scale CO in the northern hemisphere (Figure 7) compared to experiment (1)
507 with column assimilation. However, assimilating profile products can have different vertical
508 impacts from assimilating column products (figure 6). Profile assimilation can out-perform column
509 assimilations in fire-impacted regions and near the surface (Figure 10).

510 Assimilating profile products tends to have a larger change to the emissions compared to
511 only assimilating column products. Simulations using emissions from profile assimilation
512 experiments in general perform better than column assimilation especially near the surface and at
513 fire source regions.

514

515 **7.3 Assimilating multispectral product versus assimilating TIR and NIR separately**

516 For multispectral/joint products, we also compare the impacts of assimilating the joint
517 product directly versus assimilating the single spectral products separately. MOPITT column JNT
518 products are retrieved from MOPITT column TIR and column NIR products, while MOPITT
519 profile JNT products are retrieved from MOPITT profile TIR and NIR products. Therefore, we
520 compare Experiment (1) to Experiment (4), Experiment (2) to Experiment (5) for demonstration.
521 In general, assimilating multispectral/joint products result in similar or slight better agreement with
522 observations compared to assimilating the single-spectral products separately. This is the case for
523 both assimilating profile products (Experiments (2) versus (5)) and column products (Experiments
524 (1) versus (4)). In addition, assimilating multispectral/joint products is more computationally
525 efficient than assimilating single spectral products separately. These two reasons point to the
526 benefit of developing multispectral/joint products for CO as well as other species such as O₃ and
527 CH₄ and assimilating them in DA systems.

528

529 **7.4 Limitation**

530 Here we only conduct experiments for 15 days due to limitation in computational
531 resources. The 15 days in July and August 2018 may not be representative of other seasons and
532 years. More research is needed to fully understand the impact of (1) assimilating multispectral/joint
533 products versus single-spectral products, (2) the comparison of satellite profiles and satellite
534 columns DA, and (3) assimilating multispectral or each product separately. Nevertheless, the
535 results and conclusions presented in this study are valid and shed light on the impacts of
536 assimilating different satellite products of the same atmospheric composition.

537 The CAM-chem+DART experiments in this study overall show improvement in
538 background and large-scale CO distributions compared to the control/spin-up run, as shown by the



539 comparisons with global observations such as TROPOMI and TCCON. However, CAM-
540 chem+DART improvement on small-scale features is challenging due to limitation in model
541 resolution, as shown by the comparisons with airborne measurements during WE-CAN. A higher
542 resolution DA system is needed to resolve these features. We are currently developing the
543 capability of DA using MUSICA+DART which will address this issue (Pfister et al., 2020).
544 MUSICA has already been shown to better resolve fires at higher resolution while still addressing
545 global-scale impacts (Tang et al., 2022, 2023).
546

547 8. Conclusions

548 We conduct 6 CAM-chem+DART assimilation runs for 15 days (July 31st, 2018 to August
549 14th, 2018) to understand the impact of (1) assimilating multispectral products versus single-
550 spectral products, (2) assimilating satellite profile products versus column products, and (3)
551 assimilating multispectral products versus assimilating individual products separately. The DA
552 runs include 1 control run that only assimilates meteorological variables and 5 experiment runs
553 that assimilate meteorological variables and different MOPITT product(s), namely (1) Column
554 JNT assimilation; (2) Profile JNT assimilation; (3) Column TIR assimilation; (4) Column TIR and
555 column NIR assimilation; and (5) Profile TIR and column NIR assimilation. We then compare the
556 results with independent CO observations from satellite, ground-based remote sensing, surface and
557 aircraft observations (TROPOMI, TCCON, CCGG sites, IAGOS, and WE-CAN). Fire and
558 anthropogenic emissions of CO are also optimized in the DA experiments. We conduct 5 CAM-
559 chem runs with the 5 sets of optimized emissions to understand the impacts of assimilating
560 different MOPITT products. We also conduct 1 additional CAM-chem runs with original
561 emissions for reference. The main findings are as follows:

562 (1) Assimilating MOPITT profile products improves model agreement with MOPITT
563 column products and vice versa.

564 (2) The five experiments show overall higher CO in the Northern Hemisphere and lower
565 CO in the tropics and India compared to the control/spin-up run.

566 (3) All five DA experiments show improved agreement with CO observations from
567 TROPOMI, TCCON, CCGG sites, and IAGOS compared to the control/spin-up run. Results were
568 not improved compared to WE-CAN because ...

569 (4) Assimilating profile products tends to have a larger change to the emissions compared
570 to only assimilating column products. The five experiments overall increase anthropogenic CO
571 emissions while reducing fire CO emissions.

572 (5) The five CAM-chem simulations with updated emissions overall show better
573 agreement with observations compared to the control run with original emissions. Simulations
574 using emissions from profile assimilation experiments in general perform better than column
575 assimilation especially near the surface and at fire source regions.

576 (6) Assimilating MOPITT joint column product leads to better model-observation
577 agreement at and near the surface than assimilating MOPITT TIR-only column product.

578 (7) Assimilating column products has larger impacts and improvement for background and
579 large-scale CO compared to assimilating profile products due to vertical localization in profile
580 assimilation. However, profile assimilation can out-perform column assimilations in fire-impacted
581 regions and near the surface.

582 (8) Assimilating multispectral/joint products result in similar or slightly better agreement
583 with observations compared to assimilating the single-spectral products separately. Assimilating
584 multispectral/joint products is also more computationally efficient than assimilating single spectral



585 products separately. Therefore, it is advantageous to develop multispectral/joint products for CO
586 as well as other species (e.g., O₃ and CH₄) and assimilating them in DA systems.

587 (9) CAM-chem+DART improvement on small-scale features is challenging due to
588 limitation in model resolution. We are currently developing the capability of DA using
589 MUSICA+DART (a higher resolution DA system) to address this issue.

590

591

592 **Competing interests**

593 At least one of the (co-)authors is a member of the editorial board of Atmospheric Measurement
594 Techniques.

595

596 **Acknowledgement**

597 This project is partially supported by NOAA Atmospheric Chemistry, Carbon Cycle and Climate
598 (AC4) Program (Award Number: NA22OAR4310204). This material is based upon work
599 supported by the National Center for Atmospheric Research, which is a major facility sponsored
600 by the National Science Foundation under Cooperative Agreement No. 1852977. We would like
601 to acknowledge high-performance computing support from Cheyenne (doi:10.5065/D6RX99HX)
602 provided by NCAR's Computational and Information Systems Laboratory, sponsored by the
603 National Science Foundation. We thank TROPOMI, TCCON, NOAA CCGG, IAGOS, and WE-
604 CAN team for observational data.

605

606 **Author contribution**

607 Conceptualization, HMW; Investigation, WT and BG; Methodology, BG, WT, HMW, and LKE;
608 Formal analysis, WT and BG; Data curation, DZ, DM, KR, and JLA; Validation, WT;
609 Visualization, WT; Supervision, HMW; Writing – original draft preparation, WT, BG, and HMW;
610 Writing – review & editing, LKE, DPE, AFA, DZ, DM, KR, and JLA.

611

612 **References**

613 Anderson, J.L., 2001. An ensemble adjustment Kalman filter for data assimilation. Monthly
614 weather review, 129(12), pp.2884-2903.

615

616 Anderson, J.L., 2003. A local least squares framework for ensemble filtering. Monthly Weather
617 Review, 131(4), pp.634-642.

618

619 Anderson, J. L., T. Hoar, K. Raeder, H. Liu, N. Collins, R. Torn and A. Arellano: The Data
620 Assimilation Research Testbed: A Community Facility. Bulletin of the American Meteorological
621 Society, 90, 1283-1296, doi:10.1175/2009BAMS2618.1, 2009.

622

623 Apituley, A., Pedernana, M., Sneep, M., Pepijn Veeffkind, J., Loyola, D., Landgraf, J., Borsdorff,
624 T., 2018. Sentinel-5 Precursor/TROPOMI Level 2 Product User Manual Carbon Monoxide,
625 SRON-S5P-LEV2-MA-002. Royal Netherlands Meteorological Institute.

626

627 Arellano Jr, A.F., Raeder, K., Anderson, J.L., Hess, P.G., Emmons, L.K., Edwards, D.P., Pfister,
628 G.G., Campos, T.L. and Sachse, G.W., 2007. Evaluating model performance of an ensemble-based
629 chemical data assimilation system during INTEX-B field mission. Atmospheric Chemistry and
630 Physics, 7(21), pp.5695-5710.



- 631
632 Barré, J., B. Gaubert, A. F. J. Arellano, H. M. Worden, D. P. Edwards, M. Deeter, J. L. Anderson,
633 K. D. Raeder, N. S. Collins, S. Tilmes, G. Francis, C. Clerbaux, L. Emmons, G. Pfister, P.-F.
634 Coheur and D. Hurtmans, 2015. Assessing the impacts of assimilating IASI and MOPITT CO
635 retrievals using CESM-CAM-chem and DART. *Journal of Geophysical Research: Atmospheres*,
636 120, no. 19, doi:10.1002/2015JD023467
637
638 Borsdorff, T., Aan de Brugh, J., Hu, H., Aben, I., Hasekamp, O., & Landgraf, J. (2018). Measuring
639 carbon monoxide with TROPOMI: First results and a comparison with ECMWF-IFS analysis data.
640 *Geophysical Research Letters*, 45(6), 2826-2832.
641
642 Borsdorff, T., Campos, T., Kille, N., Zarzana, K. J., Volkamer, R., and Landgraf, J.: Vertical
643 information of CO from TROPOMI total column measurements in context of the CAMS-IFS data
644 assimilation scheme, *Atmos. Meas. Tech.*, 16, 3027–3038, [https://doi.org/10.5194/amt-16-3027-](https://doi.org/10.5194/amt-16-3027-2023)
645 2023, 2023.
646
647 Candille, G., Côté, C., Houtekamer, P.L. and Pellerin, G.: Verification of an ensemble prediction
648 system against observations. *Monthly Weather Review*, 135(7), pp.2688-2699, 2007.
649
650 Chance, K., Liu, X., Miller, C. C., González Abad, G., Huang, G., Nowlan, C., Souri, A., Suleiman,
651 R., Sun, K., Wang, H., Zhu, L., Zoogman, P., Al-Saadi, J., Antuña-Marrero, J. C., Carr, J.,
652 Chatfield, R., Chin, M., Cohen, R., Edwards, D., Fishman, J., Flittner, D., Geddes, J., Grutter, M.,
653 Herman, J. R., Jacob, D. J., Janz, S., Joiner, J., Kim, J., Krotkov, N. A., Lefer, B., Martin, R. V.,
654 Mayol-Bracero, O. L., Naeger, A., Newchurch, M., Pfister, G. G., Pickering, K., Pierce, R. B.,
655 Rivera Cárdenas, C., Saiz-Lopez, A., Simpson, W., Spinei, E., Spurr, R. J. D., Szykman, J. J.,
656 Torres, O., and Wang, J.: TEMPO Green Paper: Chemistry, Physics, and Meteorology
657 Experiments with the Tropospheric Emissions: Monitoring of Pollution Instrument, in: *Sensors*,
658 *Systems, and Next-Generation Satellites XXIII*, Strasbourg, France, 9-12 September 2019, edited
659 by: Neeck, S. P., Kimura, T., and Martimort, P., *Proc. SPIE*, 11151, p. 10,
660 <https://doi.org/10.1117/12.2534883>, 2019.
661
662 Cuesta, J., Eremenko, M., Liu, X., Dufour, G., Cai, Z., Höpfner, M., von Clarmann, T., Sellitto,
663 P., Forêt, G., Gaubert, B. and Beekmann, M., 2013. Satellite observation of lowermost
664 tropospheric ozone by multispectral synergism of IASI thermal infrared and GOME-2 ultraviolet
665 measurements over Europe. *Atmospheric Chemistry and Physics*, 13(19), pp.9675-9693.
666
667 Danabasoglu, G., Lamarque, J.F., Bacmeister, J., Bailey, D.A., DuVivier, A.K., Edwards, J.,
668 Emmons, L.K., Fasullo, J., Garcia, R., Gettelman, A. and Hannay, C., 2020. The community earth
669 system model version 2 (CESM2). *Journal of Advances in Modeling Earth Systems*, 12(2),
670 p.e2019MS001916.
671
672 Deeter, M. N., Emmons, L. K., Francis, G. L., Edwards, D. P., Gille, J. C., Warner, J. X., Khattatov,
673 B., Ziskin, D., Lamarque, J.-F., Ho, S.-P., Yudin, V., Attie, J.-L., Packman, D., Chen, J., Mao, D.,
674 and Drummond, J. R.: Operational carbon monoxide retrieval algorithm and selected results for
675 the MOPITT instrument, *J. Geophys. Res.*, 108(D14), 4399, doi:10.1029/2002JD003186, 2003.
676



- 677 Deeter, M. N., Worden, H. M., Gille, J. C., Edwards, D. P., Mao, D., and Drummond, J. R.:
678 MOPITT multispectral CO retrievals: Origins and effects of geophysical radiance errors, J.
679 Geophys. Res., 116, D15303, doi:10.1029/2011JD015703, 2011.
680
- 681 Deeter, M. N., Martínez-Alonso, S., Edwards, D. P., Emmons, L. K., Gille, J. C., Worden, H. M.,
682 Pittman, J. V., Daube, B. C., and Wofsy, S. C.: Validation of MOPITT Version 5 thermalinfrared,
683 near-infrared, and multispectral carbon monoxide profile retrievals for 2000–2011, J. Geophys.
684 Res., 118, 6710–6725, doi:10.1002/jgrd.50272, 2013.
685
- 686 Deeter, M., Francis, G., Gille, J., Mao, D., Martínez-Alonso, S., Worden, H., Ziskin, D.,
687 Drummond, J., Commane, R., Diskin, G., and McKain, K.: The MOPITT Version 9 CO product:
688 sampling enhancements and validation, Atmos. Meas. Tech., 15, 2325–2344,
689 <https://doi.org/10.5194/amt-15-2325-2022>, 2022.
690
- 691 Emmons, L. K., Schwantes, R. H., Orlando, J. J., Tyndall, G., Kinnison, D., Lamarque, J.-F., et al.
692 (2020). The chemistry mechanism in the Community Earth System Model version 2 (CESM2).
693 Journal of Advances in Modeling Earth Systems, 12(4), e2019MS001882.
694 <https://doi.org/10.1029/2019MS001882>.
695
- 696 Flynn, L., et al. (2014), Performance of the Ozone Mapping and Profiler Suite (OMPS) products,
697 *J. Geophys. Res. Atmos.*, 119, 6181–6195, doi:[10.1002/2013JD020467](https://doi.org/10.1002/2013JD020467).
698
- 699 Fu, D., Bowman, K. W., Worden, H. M., Natraj, V., Worden, J. R., Yu, S., Veeffkind, P., Aben, I.,
700 Landgraf, J., Strow, L., and Han, Y.: High-resolution tropospheric carbon monoxide profiles
701 retrieved from CrIS and TROPOMI, Atmos. Meas. Tech., 9, 2567–2579,
702 <https://doi.org/10.5194/amt-9-2567-2016>, 2016.
703
- 704 Fu, D., Kulawik, S. S., Miyazaki, K., Bowman, K. W., Worden, J. R., Eldering, A., Livesey, N. J.,
705 Teixeira, J., Irion, F. W., Herman, R. L., Osterman, G. B., Liu, X., Levelt, P. F., Thompson, A.
706 M., and Luo, M.: Retrievals of tropospheric ozone profiles from the synergism of AIRS and OMI:
707 methodology and validation, Atmos. Meas. Tech., 11, 5587–5605, <https://doi.org/10.5194/amt-11-5587-2018>, 2018.
708
- 709
- 710 Gaubert, B., Coman, A., Foret, G., Meleux, F., Ung, A., Rouil, L., Ionescu, A., Candau, Y., and
711 Beekmann, M.: Regional scale ozone data assimilation using an ensemble Kalman filter and the
712 CHIMERE chemical transport model, Geosci. Model Dev., 7, 283–302,
713 <https://doi.org/10.5194/gmd-7-283-2014>, 2014.
714
- 715 Gaubert, B., Arellano, A. F., Barré, J., Worden, H. M., Emmons, L. K., Tilmes, S., Buchholz, R.
716 R., Vitt, F., Raeder, K., Collins, N., Anderson, J. L., Wiedinmyer, C., Martínez-Alonso, S.,
717 Edwards, D. P., Andreae, M. O., Hannigan, J. W., Petri, C., Strong, K., and Jones, N.: Toward a
718 chemical reanalysis in a coupled chemistry-climate model: An evaluation of MOPITT CO
719 assimilation and its impact on tropospheric composition, J. Geophys. Res.-Atmos., 121, 7310–
720 7343, <https://doi.org/10.1002/2016JD024863>, 2016.
721



- 722 Gaubert, B., Worden, H. M., Arellano, A. F. J., Emmons, L. K., Tilmes, S., Barré, J., Martinez
723 Alonso, S., Vitt, F., Anderson, J. L., Alkemade, F., Houweling, S., and Edwards, D. P.: Chemical
724 feedback from decreasing carbon monoxide emissions. *Geophys. Res. Lett.*, 44, 9985–9995,
725 <https://doi.org/10.1002/2017GL074987>, 2017.
- 726
- 727 Gaubert, B., Emmons, L. K., Raeder, K., Tilmes, S., Miyazaki, K., Arellano Jr., A. F., Elguindi,
728 N., Granier, C., Tang, W., Barré, J., Worden, H. M., Buchholz, R. R., Edwards, D. P., Franke, P.,
729 Anderson, J. L., Saunio, M., Schroeder, J., Woo, J.-H., Simpson, I. J., Blake, D. R., Meinardi, S.,
730 Wennberg, P. O., Crounse, J., Teng, A., Kim, M., Dickerson, R. R., He, H., Ren, X., Pusede, S.
731 E., and Diskin, G. S.: Correcting model biases of CO in East Asia: impact on oxidant distributions
732 during KORUS-AQ, *Atmos. Chem. Phys.*, 20, 14617–14647, <https://doi.org/10.5194/acp-20-14617-2020>, 2020.
- 733
- 734
- 735 Gaubert, B., Edwards, D. P., Anderson, J. L., Arellano, A.F., Barré, J., Buchholz, R.R., Darras, S.,
736 Emmons, L.K., Fillmore, D., Granier, C., et al. Global Scale Inversions from MOPITT CO and
737 MODIS AOD. *Remote Sens.* 2023,15,4813. <https://doi.org/10.3390/rs15194813>
- 738
- 739 Inness, A., M. Ades, A. Agustí-Panareda, J. Barré, A. Benedictow, A.-M. Blechschmidt, J. J.
740 Dominguez, R. Engelen, H. Eskes, J. Flemming, V. Huijnen, L. Jones, Z. Kipling, S. Massart, M.
741 Parrington, V.-H. Peuch, M. Razinger, S. Remy, M. Schulz, and M. Suttie (2019), The CAMS
742 reanalysis of atmospheric composition, *Atmospheric Chemistry and Physics*, 19(6), 35153556,
743 doi:<https://doi.org/10.5194/acp-19-3515-2019>.
- 744
- 745 Inness, A., I. Aben, M. Ades, T. Borsdorff, J. Flemming, L. Jones, J. Landgraf, B. Langerock, P.
746 Nedelec, M. Parrington, and R. Ribas (2022), Assimilation of S5P/TROPOMI carbon monoxide
747 data with the global CAMS near-real-time system, *Atmospheric Chemistry and Physics*, 22(21),
748 1435514376, doi:[10.5194/acp-22-14355-2022](https://doi.org/10.5194/acp-22-14355-2022).
- 749
- 750 Jiang, Z., Jones, D. B. A., Worden, H. M., Deeter, M. N., Henze, D. K., Worden, J., Bowman, K.
751 W., Brenninkmeijer, C. A. M., and Schuck, T. J.: Impact of model errors in convective transport
752 on CO source estimates inferred from MOPITT CO retrievals, *J. Geophys. Res.-Atmos.*, 118,
753 2073–2083, <https://doi.org/10.1002/jgrd.50216>, 2013.
- 754
- 755 Jiang, Z., Worden, J. R., Worden, H., Deeter, M., Jones, D. B. A., Arellano, A. F., and Henze, D.
756 K.: A 15-year record of CO emissions constrained by MOPITT CO observations, *Atmos. Chem.*
757 *Phys.*, 17, 4565–4583, <https://doi.org/10.5194/acp-17-4565-2017>, 2017.
- 758
- 759 Kim, J., Jeong, U., Ahn, M.-H., Kim, J. H., Park, R. J., Lee, H., Song, C. H., Choi, Y.-S., Lee, K.-
760 H., Yoo, J.-M., Jeong, M.-J., Park, S. K., Lee, K.-M., Song, C.-K., Kim, S.-W., Kim, Y. J., Kim,
761 S.-W., Kim, M., Go, S., Liu, X., Chance, K., Chan Miller, C., Al-Saadi, J., Veihelmann, B.,
762 Bhartia, P. K., Torres, O., Abad, G. G., Haffner, D. P., Ko, D. H., Lee, S. H., Woo, J.-H., Chong,
763 H., Park, S. S., Nicks, D., Choi, W. J., Moon, K.-J., Cho, A., Yoon, J., Kim, S.-k., Hong, H., Lee,
764 K., Lee, H., Lee, S., Choi, M., Veeffkind, P., Levelt, P. F., Edwards, D. P., Kang, M., Eo, M., Bak,
765 J., Baek, K., Kwon, H.-A., Yang, J., Park, J., Han, K. M., Kim, B.-R., Shin, H.-W., Choi, H., Lee,
766 E., Chong, J., Cha, Y., Koo, J.-H., Irie, H., Hayashida, S., Kasai, Y., Kanaya, Y., Liu, C., Lin, J.,
767 Crawford, J. H., Carmichael, G. R., Newchurch, M. J., Lefer, B. L., Herman, J. R., Swap, R. J.,



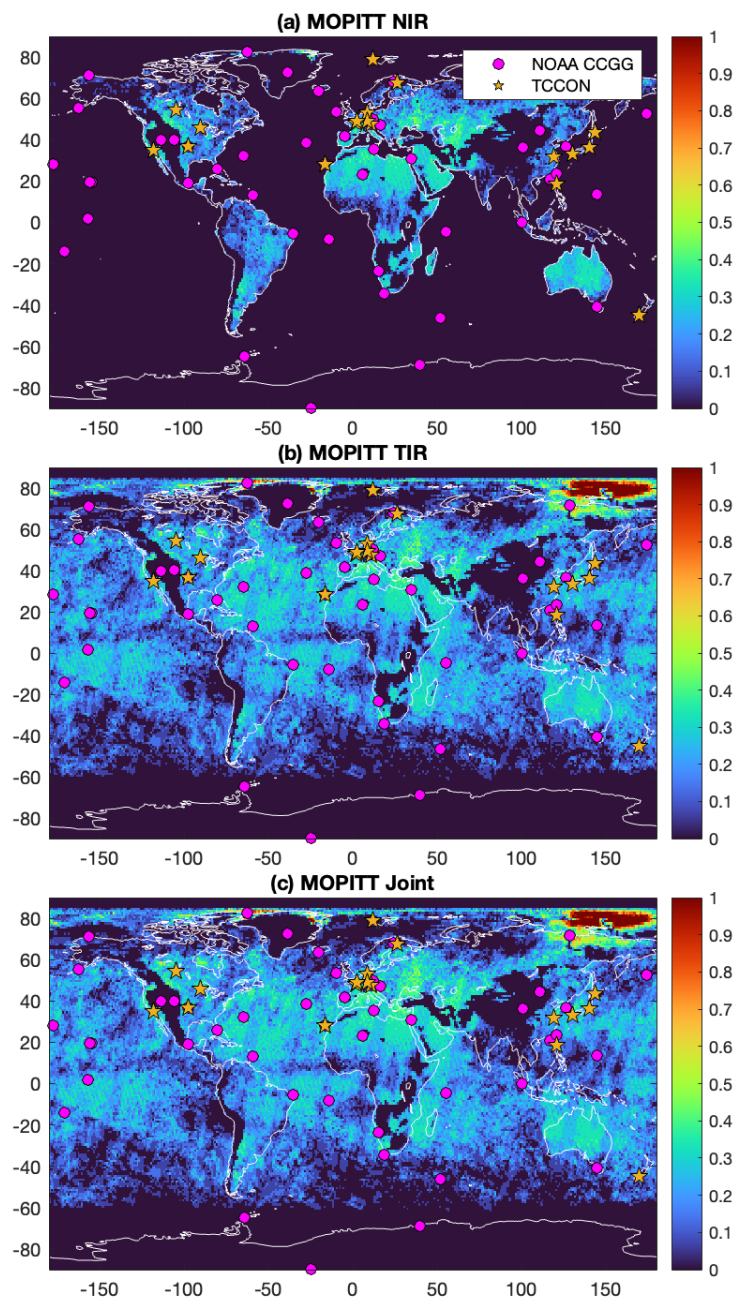
- 768 Lau, A. K. H., Kurosu, T. P., Jaross, G., Ahlers, B., Dobber, M., McElroy, C. T., and Choi, Y.:
769 New Era of Air Quality Monitoring from Space: Geostationary Environment Monitoring
770 Spectrometer (GEMS), *B. Am. Meteorol. Soc.*, 101, E1–E22, [https://doi.org/10.1175/bams-d-18-](https://doi.org/10.1175/bams-d-18-0013.1)
771 0013.1, 2020.
772
- 773 Levelt, P. F., Joiner, J., Tamminen, J., Veefkind, J. P., Bhartia, P. K., Stein Zweers, D. C., Duncan,
774 B. N., Streets, D. G., Eskes, H., van der A, R., McLinden, C., Fioletov, V., Carn, S., de Laat, J.,
775 DeLand, M., Marchenko, S., McPeters, R., Ziemke, J., Fu, D., Liu, X., Pickering, K., Apituley,
776 A., González Abad, G., Arola, A., Boersma, F., Chan Miller, C., Chance, K., de Graaf, M.,
777 Hakkarainen, J., Hassinen, S., Ialongo, I., Kleipool, Q., Krotkov, N., Li, C., Lamsal, L., Newman,
778 P., Nowlan, C., Suleiman, R., Tilstra, L. G., Torres, O., Wang, H., and Wargan, K.: The Ozone
779 Monitoring Instrument: overview of 14 years in space, *Atmos. Chem. Phys.*, 18, 5699–5745,
780 <https://doi.org/10.5194/acp-18-5699-2018>, 2018.
781
- 782 Liu, X., Ma, P.-L., Wang, H., Tilmes, S., Singh, B., Easter, R. C., et al. (2016b). Description and
783 evaluation of a new four-mode version of the Modal Aerosol Module (MAM4) within version 5.3
784 of the Community Atmosphere Model. *Geoscientific Model Development*, 9, 505–522.
785 <https://doi.org/10.5194/gmd-9-505-2016>.
786
- 787 Ménard, R. and Chang, L.P.: Assimilation of stratospheric chemical tracer observations using a
788 Kalman filter. Part II: χ^2 -validated results and analysis of variance and correlation dynamics.
789 *Monthly weather review*, 128(8), pp.2672-2686, [https://doi.org/10.1175/1520-](https://doi.org/10.1175/1520-0493(2000)128<2672:AOSCTO>2.0.CO;2)
790 [0493\(2000\)128<2672:AOSCTO>2.0.CO;2](https://doi.org/10.1175/1520-0493(2000)128<2672:AOSCTO>2.0.CO;2), 2000.
791
- 792 Mettig, N., Weber, M., Rozanov, A., Burrows, J. P., Veefkind, P., Thompson, A. M., Stauffer, R.
793 M., Leblanc, T., Ancellet, G., Newchurch, M. J., Kuang, S., Kivi, R., Tully, M. B., Van Malderen,
794 R., Piters, A., Kois, B., Stübi, R., and Skrivankova, P.: Combined UV and IR ozone profile
795 retrieval from TROPOMI and CrIS measurements, *Atmos. Meas. Tech.*, 15, 2955–2978,
796 <https://doi.org/10.5194/amt-15-2955-2022>, 2022.
797
- 798 Natraj V., X. Liu, S. Kulawik, K. Chance, R. Chatfield, D.P. Edwards, A. Eldering, G. Francis, T.
799 Kurosu, K. Pickering, R. Spurr, and H. M. Worden. Multi-spectral sensitivity studies for the
800 retrieval of tropospheric and lowermost tropospheric ozone from simulated clear-sky geo-cape
801 measurements *Atmos. Environ.*, 45, 7151-7165. <https://doi.org/10.1016/j.atmosenv.2011.09.014>,
802 2011.
803
- 804 Petron, G., Crotwell, A.M., Crotwell, M.J., Dlugokencky, E., Madronich, M., Moglia, E., Neff,
805 D., Thoning, K., Wolter, S., Mund, J.W. (2022), Atmospheric Carbon Monoxide Dry Air Mole
806 Fractions from the NOAA GML Carbon Cycle Cooperative Global Air Sampling Network, 1988-
807 2021, Version: 2022-07-28, <https://doi.org/10.15138/33bv-s284>.
808
- 809 Peuch, V. H., Engelen, R., Rixen, M., Dee, D., Flemming, J., Suttie, M., ... & Thépaut, J. N. (2022).
810 The copernicus atmosphere monitoring service: From research to operations. *Bulletin of the*
811 *American Meteorological Society*, 103(12), E2650-E2668. [https://doi.org/10.1175/BAMS-D-21-](https://doi.org/10.1175/BAMS-D-21-0314.1)
812 [0314.1](https://doi.org/10.1175/BAMS-D-21-0314.1)
813



- 814 Pfister, G., Eastham, S., Arellano, A. F., Aumont, B., Barsanti, K., Barth, M., Conley, A., Davis,
815 N., Emmons, L., Fast, J., Fiore, A., Gaubert, B., Goldhaber, S., Granier, C., Grell, G., Guevara,
816 M., Henze, D., Hodzic, A., Liu, X., Marsh, D., Orlando, J., Plane, J., Polvani, L., Rosenlof, K.,
817 Steiner, A., Jacob, D., and Brasseur, G.: The Multi-Scale Infrastructure for Chemistry and Aerosols
818 (MUSICA), *B. Am. Meteorol. Soc.*, 101, E1743–E1760, [https://doi.org/10.1175/bams-d-19-](https://doi.org/10.1175/bams-d-19-0331.1)
819 [0331.1](https://doi.org/10.1175/bams-d-19-0331.1), 2020.
- 820
- 821 Petzold, A., Thouret, V., Gerbig, C., Zahn, A., Brenninkmeijer, C.A., Gallagher, M., Hermann,
822 M., Pontaud, M., Ziereis, H., Boulanger, D. and Marshall, J., 2015. Global-scale atmosphere
823 monitoring by in-service aircraft—current achievements and future prospects of the European
824 Research Infrastructure IAGOS. *Tellus B: Chemical and Physical Meteorology*, 67(1), p.28452.
- 825
- 826 Raeder, K, J. L., Anderson, N. Collins, T. J. Hoar, J. E. Kay, P. H., Lauritzen and R. Pincus, 2012
827 DART/CAM: An Ensemble Data Assimilation for CESM Atmospheric Models. *Journal of*
828 *Climate*, 25, 6304–6317, doi:10.1175/JCLI-D-11-00395.1.
- 829
- 830 Raeder, K., Hoar, T. J., El-Gharamti, M., Johnson, B. K., Collins, N., Anderson, J. L., Steward, J.,
831 Coady, M. A new CAM6 + DART reanalysis with surface forcing from CAM6 to other CESM
832 models. *Scientific Reports* 2021, 11. <https://doi.org/10.1038/s41598-021-92927-0>.
- 833
- 834 Schneider, M., Ertl, B., Tu, Q., Diekmann, C.J., Khosrawi, F., Röhling, A.N., Hase, F., Dubravica,
835 D., García, O.E., Sepúlveda, E. and Borsdorff, T., 2022. Synergetic use of IASI profile and
836 TROPOMI total-column level 2 methane retrieval products. *Atmospheric Measurement*
837 *Techniques*, 15(14), pp.4339–4371.
- 838
- 839 Sekiya, T., Miyazaki, K., Ogochi, K., Sudo, K., Takigawa, M., Eskes, H. and Boersma, K.F., 2021.
840 Impacts of horizontal resolution on global data assimilation of satellite measurements for
841 tropospheric chemistry analysis. *Journal of Advances in Modeling Earth Systems*, 13(6),
842 p.e2020MS002180.
- 843
- 844 Soulie, A., C. Granier, S. Darras, N. Zilbermann, T. Doumbia, M. Guevara, J.-P. Jalkanen, S.
845 Keita, C. Lioussé, M. Crippa, D. Guizzardi, R. Hoesly, S. J. Smith, Global Anthropogenic
846 Emissions (CAMS-GLOB-ANT) for the Copernicus Atmosphere Monitoring Service Simulations
847 of Air Quality Forecasts and Reanalyses, submitted to *Earth Syst. Sci. Data*, paper *essd-2023-306*,
848 2023.
- 849
- 850 Tang, W., Emmons, L.K., Buchholz, R.R., Wiedinmyer, C., Schwantes, R.H., He, C., Kumar, R.,
851 Pfister, G.G., Worden, H.M., Hornbrook, R.S. and Apel, E.C., 2022. Effects of fire diurnal
852 variation and plume rise on US Air quality during FIREX-AQ and WE-CAN Based on the multi-
853 scale infrastructure for chemistry and aerosols (MUSICAv0). *Journal of Geophysical Research:*
854 *Atmospheres*, 127(16), p.e2022JD036650.
- 855
- 856 Tang, W., Pfister, G.G., Kumar, R., Barth, M., Edwards, D.P., Emmons, L.K. and Tilmes, S., 2023.
857 Capturing High-Resolution Air Pollution Features Using the Multi-Scale Infrastructure for
858 Chemistry and Aerosols Version 0 (MUSICAv0) Global Modeling System. *Journal of*
859 *Geophysical Research: Atmospheres*, 128(7), p.e2022JD038345.



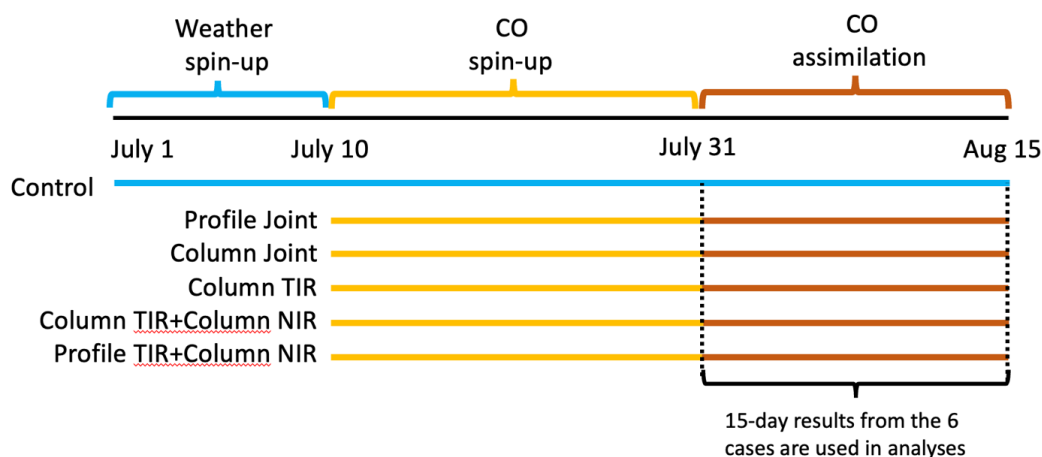
860
861 Total Carbon Column Observing Network (TCCON) Team. (2022). 2020 TCCON Data Release
862 (Version GGG2020) [Data set]. CaltechDATA. <https://doi.org/10.14291/TCCON.GGG2020>.
863
864 Tilmes, S., Hodzic, A., Emmons, L. K., Mills, M. J., Gettelman, A., Kinnison, D. E., et al. (2019).
865 Climate forcing and trends of organic aerosols in the Community Earth System Model (CESM2).
866 Journal of Advances in Modeling Earth Systems, 11(12), 4323–4351.
867 <https://doi.org/10.1029/2019MS00182>.
868
869 Total Carbon Column Observing Network (TCCON) Team. (2022). 2020 TCCON Data Release
870 (Version GGG2020) [Data set]. CaltechDATA. <https://doi.org/10.14291/TCCON.GGG2020>.
871
872 Veefkind, J. P., Aben, I., McMullan, K., Förster, H., De Vries, J., Otter, G., ... & Levelt, P. F.
873 (2012). TROPOMI on the ESA Sentinel-5 Precursor: A GMES mission for global observations of
874 the atmospheric composition for climate, air quality and ozone layer applications. Remote Sensing
875 of Environment, 120, 70-83.
876
877 Wiedinmyer, C., Kimura, Y., McDonald-Buller, E. C., Emmons, L. K., Buchholz, R. R., Tang,
878 W., Seto, K., Joseph, M. B., Barsanti, K. C., Carlton, A. G., and Yokelson, R.: The Fire Inventory
879 from NCAR version 2.5: an updated global fire emissions model for climate and chemistry
880 applications, Geosci. Model Dev., 16, 3873–3891, <https://doi.org/10.5194/gmd-16-3873-2023>,
881 2023.
882
883 Worden, H.M., Logan, J.A., Worden, J.R., Beer, R., Bowman, K., Clough, S.A., Eldering, A.,
884 Fisher, B.M., Gunson, M.R., Herman, R.L. and Kulawik, S.S., 2007. Comparisons of Tropospheric
885 Emission Spectrometer (TES) ozone profiles to ozonesondes: Methods and initial results. Journal
886 of Geophysical Research: Atmospheres, 112(D3).
887
888 Worden, H. M., Deeter, M. N., Edwards, D. P., Gille, J. C., Drummond, J. R., and Nédélec, P.:
889 Observations of near-surface carbon monoxide from space using MOPITT multispectral retrievals,
890 J. Geophys. Res., 115, D18314, <https://doi.org/10.1029/2010JD014242>, 2010.
891
892 Zeng, Z.-C., Lee, L., and Qi, C.: Diurnal carbon monoxide observed from a geostationary infrared
893 hyperspectral sounder: first result from GIIRS on board FengYun-4B, Atmos. Meas. Tech., 16,
894 3059–3083, <https://doi.org/10.5194/amt-16-3059-2023>, 2023.
895
896
897
898
899
900



901 **Figure 1.** Daily number of super-observations per day and per grid from MOPITT (a) TIR, (b)
902 NIR, and (c) JNT products during July 16th 2018 to August 14th 2018. Total Carbon Column
903 Observing Network (TCCON) sites are marked by yellow stars and NOAA Carbon Cycle
904 Greenhouse Gases (CCGG) sites are marked by pink circles.
905
906

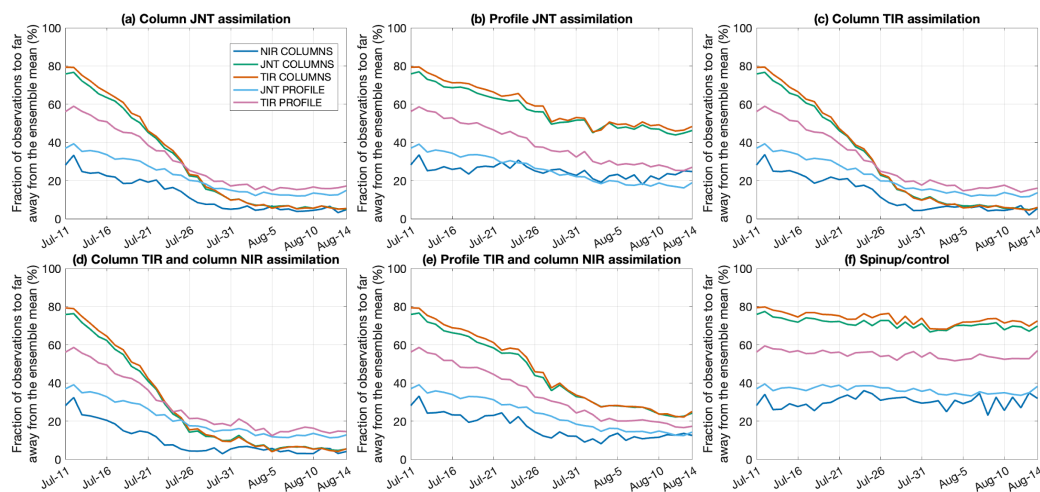


907



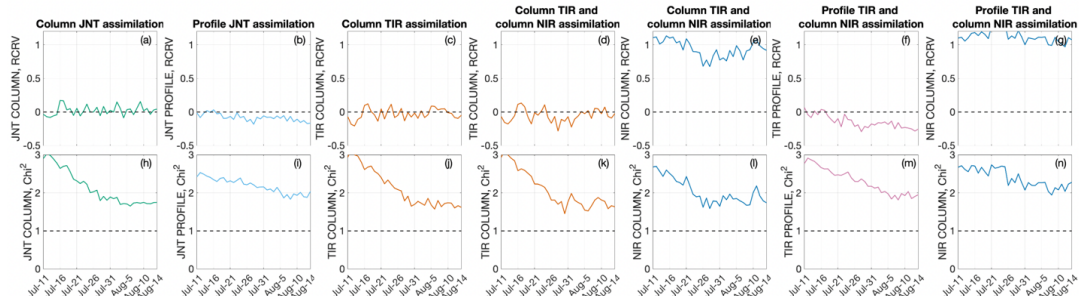
908
 909
 910
 911
 912
 913
 914
 915
 916

Figure 2. Setup of the CAM-chem/DART data assimilation experiments.



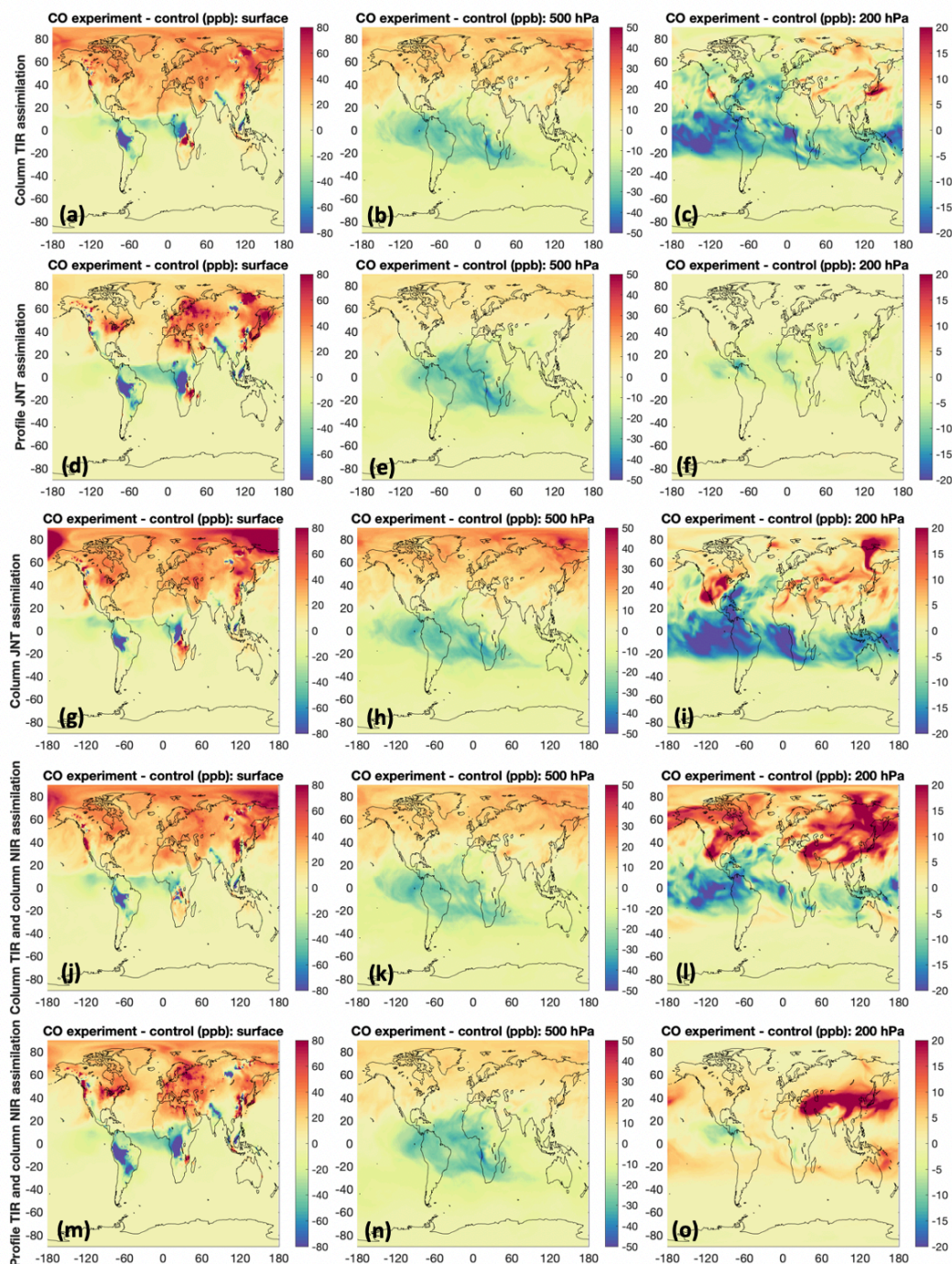
917
 918
 919
 920
 921

Figure 3. Time series of the fractions of observations rejected by the assimilation system (%) due to that they are too far from the ensemble mean.



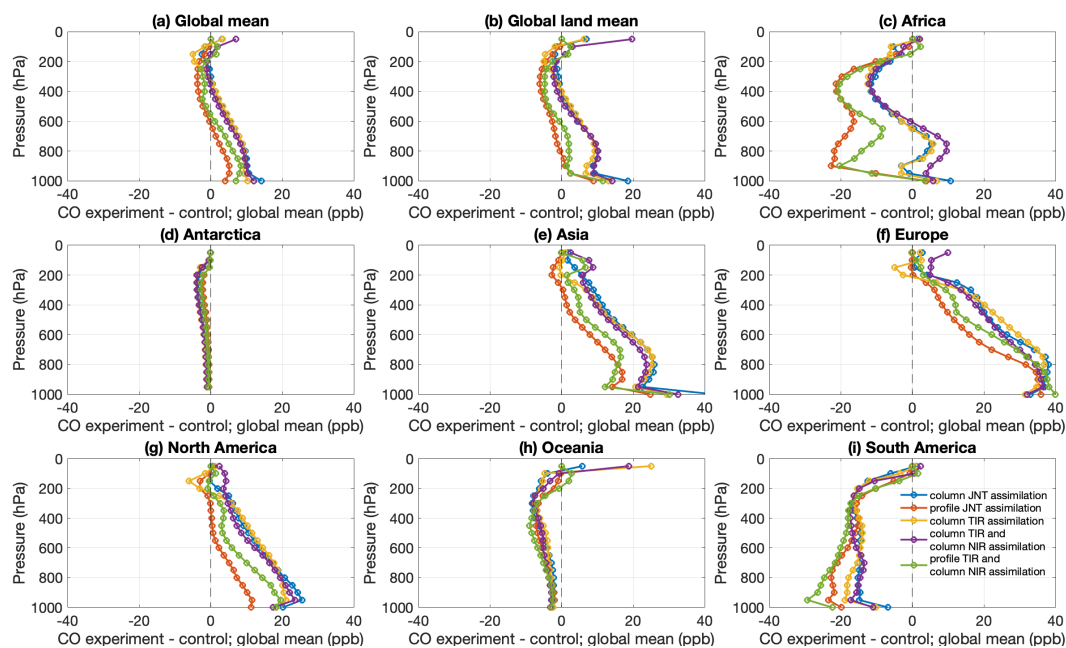
922
923 **Figure 4.** timeseries of (a-g) daily mean of Reduced Centered Random Variable (RCRV) and (h-
924 n) daily mean of Chi-square. For each experiment, only RCRV and Chi-square of the MOPITT
925 product that were assimilated are shown.

926
927
928



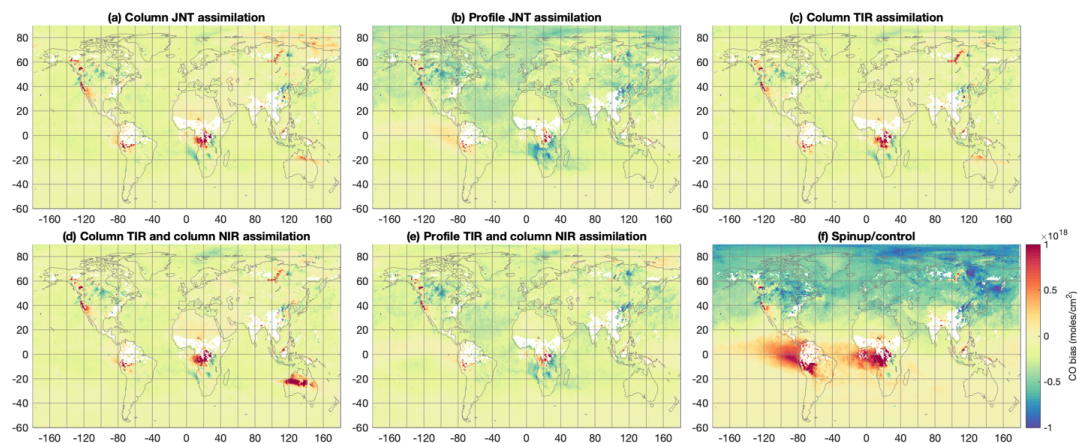
929
 930
 931

Figure 5. 15-day (July 31 - August 14, 2018) average of the difference in CO (forecast of experiment minus control run) for the 5 experiments at the model surface, 500 hPa, and 200 hPa.



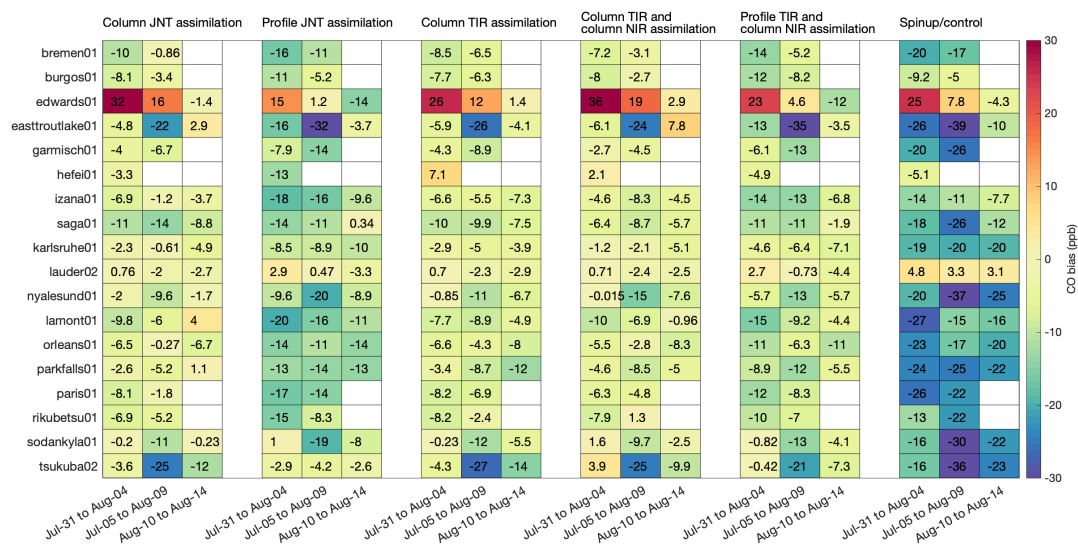
932
 933
 934
 935
 936
 937

Figure 6. Vertical profile of the 15-day (July 31 - August 14, 2018) average difference in CO (forecast of experiment minus control run) over different regions.



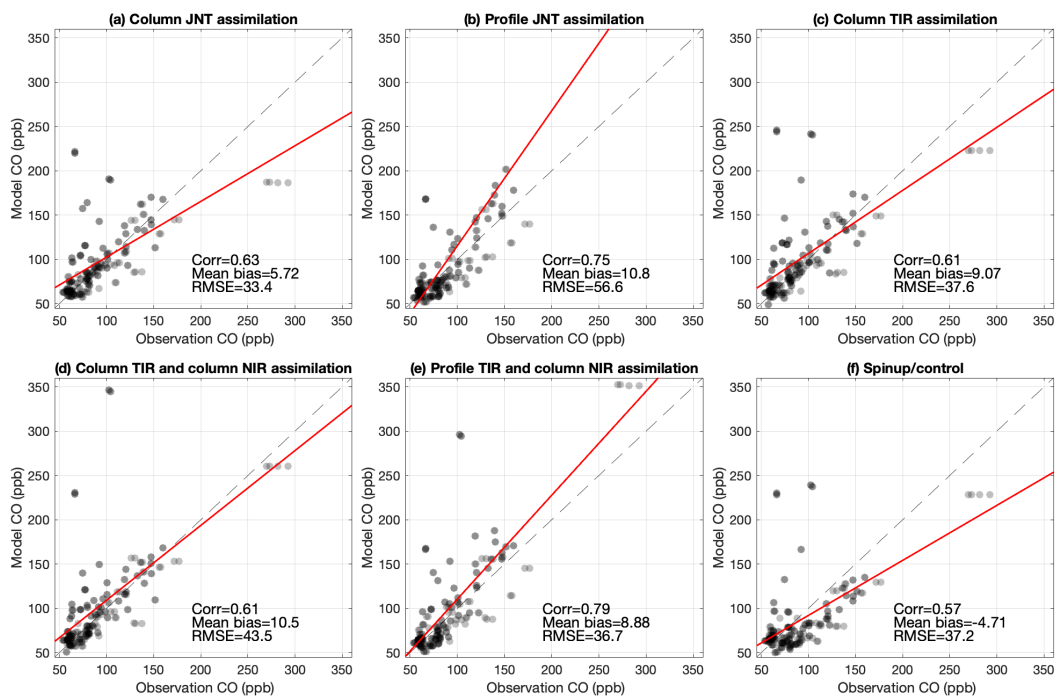
938
 939
 940
 941
 942
 943

Figure 7. 15-day (July 31 - August 14, 2018) mean biases (ppb) of modeled CO against CO columns from the TROPospheric Monitoring Instrument (TROPOMI) for the 5 experiments and the control run. TROPOMI averaging kernels are applied to model CO for the comparisons.



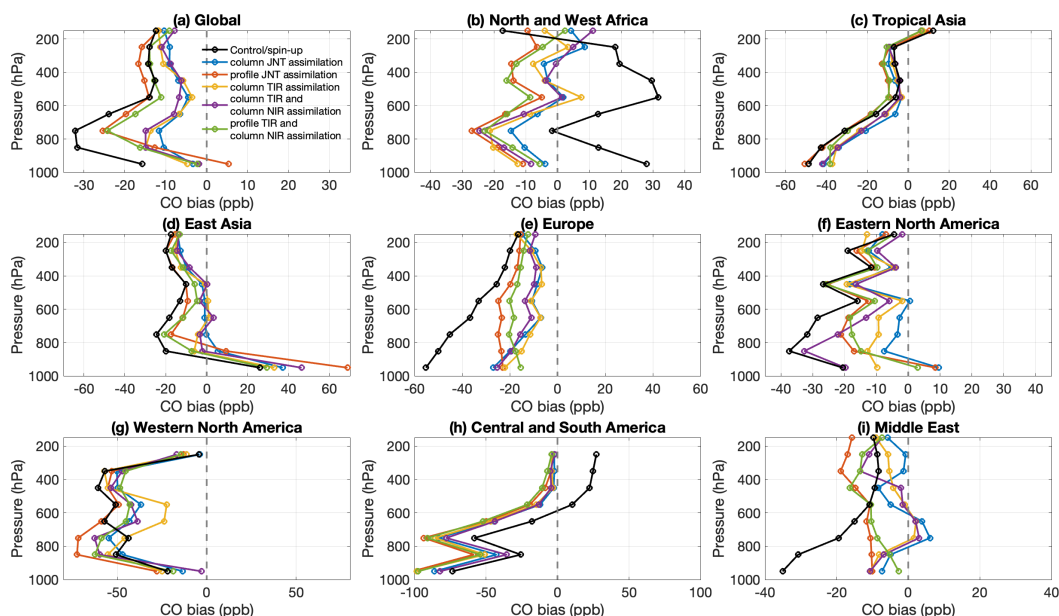
944
 945
 946
 947
 948
 949
 950
 951
 952

Figure 8. Mean biases (ppb) of modeled CO against CO columns from the Total Carbon Column Observing Network (TCCON) for the 5 experiment and the control run. TCCON averaging kernels are applied to model CO for the comparisons. Spatial locations of TCCON sites can be found in Figure 2 and Figure S1. A time series of TCCON and modeled CO can be found in Figure S4.



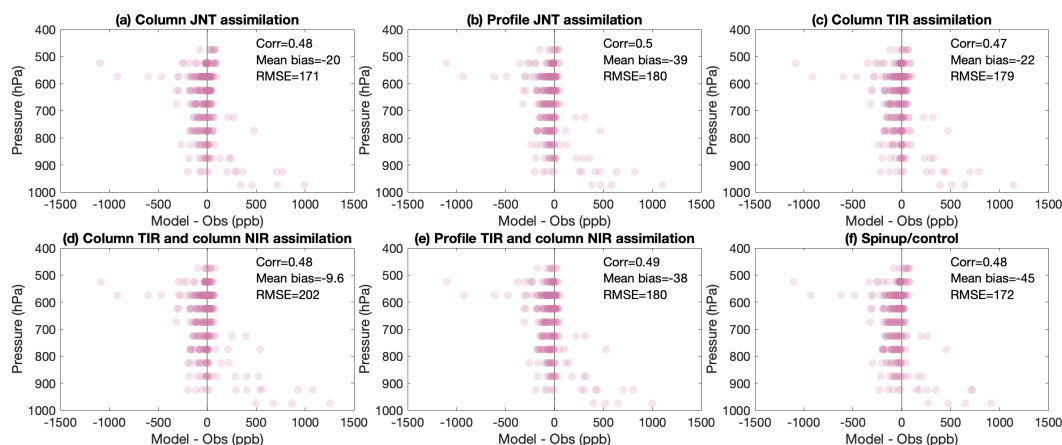
953
954
955
956
957
958
959
960

Figure 9. Comparisons of modeled CO (ppb) and CO observations from the NOAA Carbon Cycle Greenhouse Gases (CCGG) sites during July 31st, 2018 to August 14th, 2018 for the 5 experiments and the control run. Spatial locations of CCGG sites can be found in Figure 2 and Figure S1. A spatial distribution of model bias in CO against CO observations from CCGG sites can be found in Figure S5.



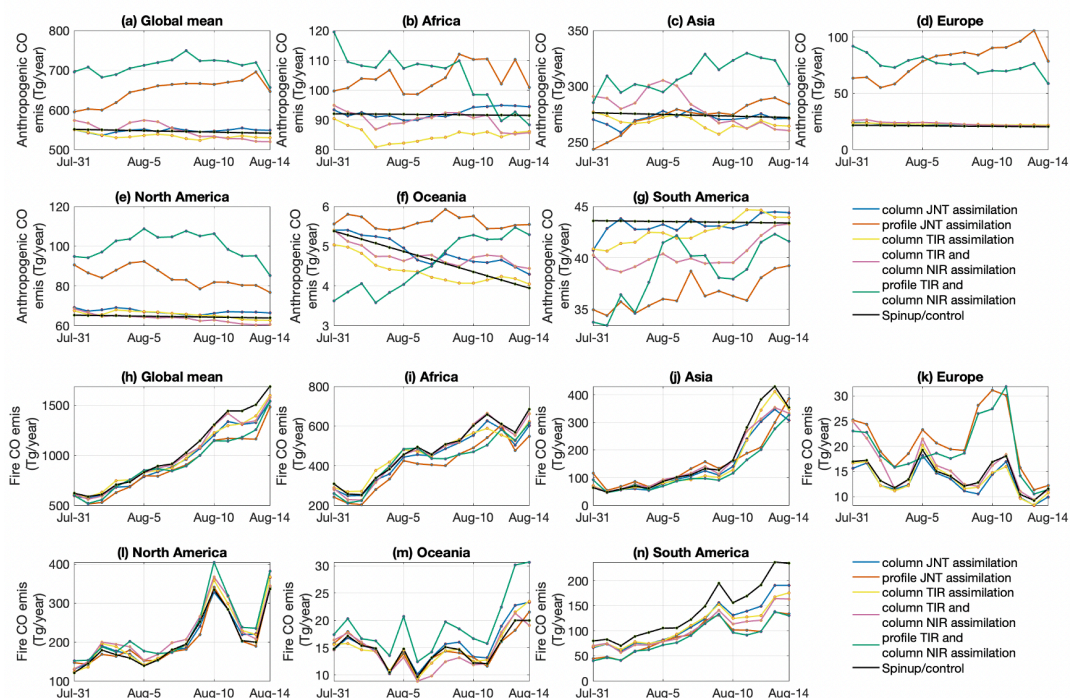
961
 962
 963
 964
 965
 966
 967

Figure 10. Mean biases (ppb) of modeled CO against CO profiles from the In-service Aircraft for a Global Observing System (IAGOS) measurements for the 5 experiments (colored lines) and the control run (black line) at different vertical levels. Locations of IAGOS CO profiles can be found in Figure S2.



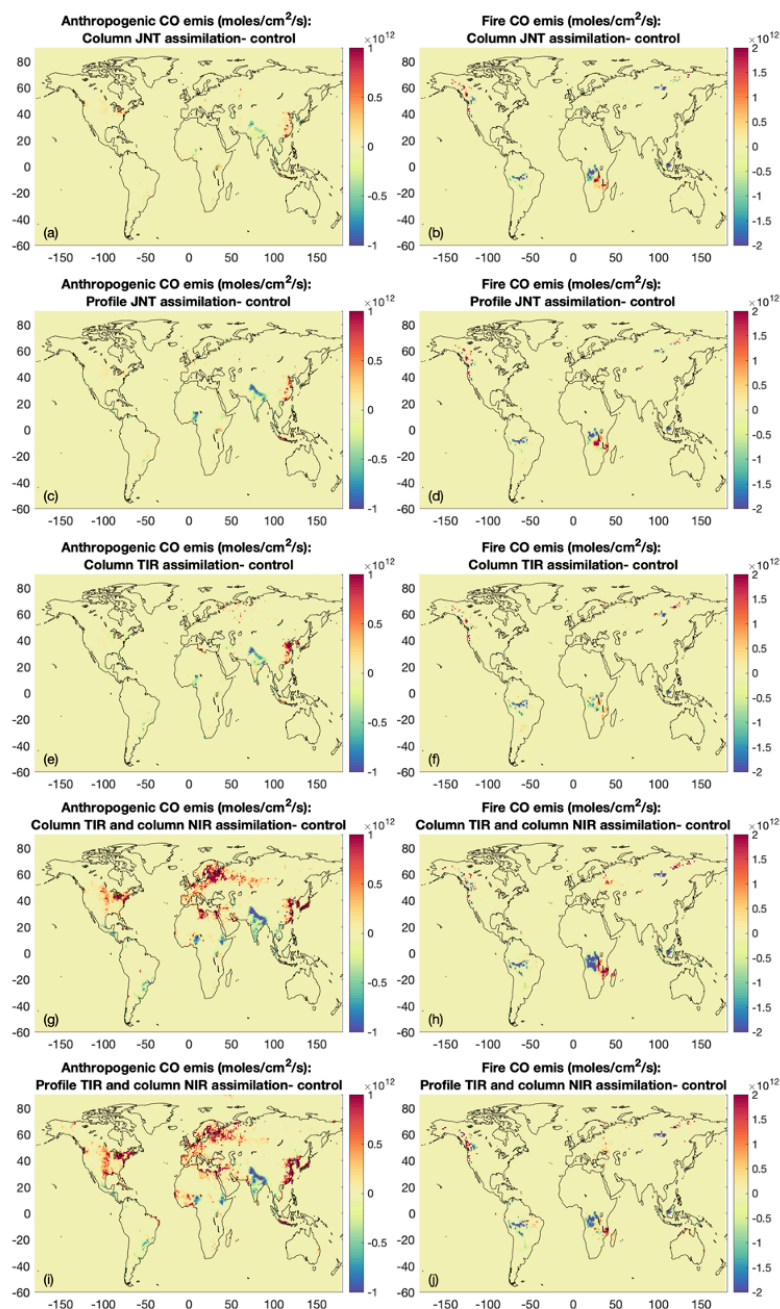
968
 969
 970
 971
 972
 973

Figure 11. Mean biases (ppb) of modeled CO against airborne CO observations from the Western wildfire Experiment for Cloud chemistry, Aerosol absorption and Nitrogen (WE-CAN) field campaign for the 5 experiments and the control run at different vertical levels.



974
975
976
977

Figure 12. Updated (a-g) CAMS anthropogenic CO emissions and (h-n) FINNv2.4 fire CO emissions as a result of assimilating different MOPITT products. The emissions from the Spinup/control run are the unchanged original emissions of CAMS and FINNv2.4.



978
979
980
981
982

Figure 13. Updates on the (a) CAMS anthropogenic CO emissions and (b) FINNv2.4 fire CO emissions as a result of assimilating MOPITT Column JNT product. Updates is calculated as CO from the experiment minus CO from the control run. (c-j) are similar to (a-b) but for other experiments.